

Quantum interference in an asymmetric Mach-Zehnder interferometer

This content has been downloaded from IOPscience. Please scroll down to see the full text.

2016 J. Opt. 18 085201

(<http://iopscience.iop.org/2040-8986/18/8/085201>)

View [the table of contents for this issue](#), or go to the [journal homepage](#) for more

Download details:

IP Address: 193.205.206.85

This content was downloaded on 04/07/2016 at 21:20

Please note that [terms and conditions apply](#).

Quantum interference in an asymmetric Mach-Zehnder interferometer

A Trenti, M Borghi, M Mancinelli, H M Price, G Fontana and L Pavesi

Department of Physics, University of Trento, via Sommarive 14, Trento 38123, Italy

E-mail: alessandro.trenti@unitn.it

Received 24 March 2016, revised 17 May 2016

Accepted for publication 31 May 2016

Published 4 July 2016



CrossMark

Abstract

A re-visitation of the well known free space Mach-Zehnder interferometer is reported here. The coexistence between one-photon and two-photons interference from collinear color entangled photon pairs is investigated. This arises from an arbitrarily small unbalance in the arm transmittance. The tuning of such asymmetry is reflected in dramatic changes in the coincidence detection, revealing beatings between one particle and two particle interference patterns. In particular, the role of the losses and of the intrinsic phase imperfectness of the lossy beamsplitter are explored in a single-port excited Mach-Zehnder interferometer. This configuration is especially useful for quantum optics on a chip, where the guiding geometry forces photons to travel in the same spatial mode.

Keywords: quantum optics, quantum interferometry, color entangled photons, nonlinear optics

(Some figures may appear in colour only in the online journal)

1. Introduction

In recent years, advances in the generation of stable quantum states of light by spontaneous parametric down conversion (SPDC) allowed to reinterpret several interferometric experiments from a quantum optical point of view [1–4]. Nonclassical interference has been observed in Michelson, Mach-Zehnder (MZ), Franson and Hong Ou Mandel (HOM) geometries [5–8]. Among these, the MZ structure received growing attentions due to its scalability in modern quantum optical integrated circuits [9–11]. However, despite the simplicity of the device, not all the possibilities have been explored. In most of the cases, the symmetric configuration, where the MZ is excited at both ports of the input beam splitter, has been considered [8, 12, 13]. In this case, the photon pair is never split after the entrance beamsplitter due to HOM effect [5], thus reducing the number of indistinguishable paths leading to a coincidence detection. Furthermore, it was assumed that the propagation characteristics (transmittance, losses, etc) of the two arms of the interferometer were the same. On one hand, this simplification offers a more direct insight on the physics of the problem, but at the same time it hides the possibility to observe novel interactions between single and two photon correlations.

In this work, we revisited the classical Mach-Zehnder interferometer by assuming asymmetry and losses to enable all the different interference possibilities. In fact, we report on the realization of an interference experiment in a Mach-Zehnder device where all the symmetries are removed. A pair of 1550 nm colour-entangled photons produced by type-0 SPDC (i.e. both the down converted photons are co-polarized and collinear with the pump ones) in a crystal of periodically poled lithium niobate (PPLN) enters in the *same* input port of the interferometer. Photon antibunching (split) and bunching (*NOON*) states, are created after the first beam splitter, and the strength of their self and mutual interaction is changed by tuning the asymmetry of the transmittance between the two arms. When bunching-bunching interactions are suppressed, the coincidence detection pattern, which is monitored as a function of the time delay between the arms, shows only one particle interference fringes. On the contrary, the period of the latter is doubled when antibunching-bunching interactions cancel, creating a two particle interference pattern. When all the interactions act simultaneously, mixed patterns, showing at the same time beatings between single-photon, two-photon and Hong Ou Mandel interference, are observed. It is worth noting that, while all these interference effects have been previously reported [5, 8, 14], it has never addressed the impact of the arm and of the beamsplitter losses on their

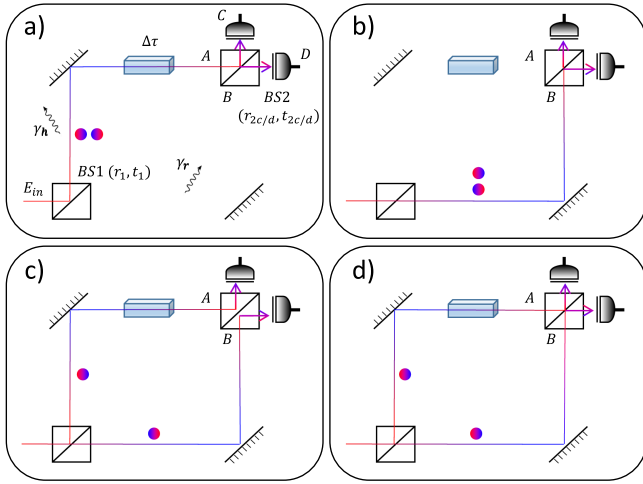


Figure 1. Panels (a, b, c, d) represent the possible paths that the photon pair can follow from $BS1$ to the output ports C and D . Cases (a) and (b) are referred as bunching states, since the photon pair is not divided by $BS1$. On the contrary, cases (c) and (d) are called antibunching states since the pair is split by $BS1$.

interplay in the same coincidence pattern. The phase imperfectness induced by the presence of the beamsplitter losses plays a role in determining the outcome of our interferometric quantum optical experiment. The assumption of a lossy beam splitter was essential to reproduce the experimental data with the theoretical model. Our treatment is particularly relevant for applications of quantum optic concepts in integrated devices, since the waveguiding geometry itself forces the two photons of the pair to travel in the same spatial direction, i.e. they are collinear at the input port of the MZ.

The paper is organized as follows: in section 2, the theoretical model of the MZ is presented, and the probability of a coincidence photodetection is derived in terms of an unbalancing parameter. The experimental setup used to validate the model predictions will be outlined in section 3. The experimental results will be discussed in section 4.

2. Model

With reference to figure 1(a), the probability per unit time of coincidence detections at the output ports C and D of the MZ at times t and $t + \tau$ is given by [15]:

$$P(\tau) = K \langle \hat{E}_D^-(t) \hat{E}_C^-(t + \tau) \hat{E}_C^+(t + \tau) \hat{E}_D^+(t) \rangle \quad (1)$$

in which K is a constant which depends on the photodetectors, while \hat{E}_C^+ and \hat{E}_D^+ are respectively the positive frequency parts of the electric field operator at the output ports C and D of the interferometer. The expectation value of expression (1) is calculated on state:

$$|\psi_{in}\rangle = |0\rangle + \frac{\beta}{\sqrt{2}} \int d\omega_s d\omega_i \phi(\omega_s, \omega_i) \hat{a}_{\omega_s}^\dagger \hat{a}_{\omega_i}^\dagger |0\rangle \quad (2)$$

which represents the two photon state produced by the SPDC. The process splits a pump photon at frequency $\tilde{\omega}$ into a signal and an idler photon at frequencies ω_s and ω_i respectively [5].

In equation (2), β is a constant which is proportional to the average number of pump photons in a second [16]. The function $\phi(\omega_s, \omega_i)$ in equation (2) is the biphoton wavefunction [16], which is normalized in such a way that $\int d\omega_s d\omega_i |\phi(\omega_s, \omega_i)|^2 = 1$. In what follows, we will consider the pump field as monochromatic, since its coherence time is assumed to greatly exceeds the one of the down converted photons. As a consequence of this approximation, we can use the energy conservation relation $\tilde{\omega} = \omega_s + \omega_i$ to express the frequency of one photon of the pair as ω , and the frequency of the twin photon as $\tilde{\omega} - \omega$. In this way, the biphoton wavefunction, which we assume to be Gaussian, can be written as:

$$\phi(\omega_s, \omega_i) \simeq \phi(\omega) = \frac{1}{\sqrt{4\pi}\sqrt{\sigma}} e^{-\frac{(\omega - \tilde{\omega}/2)^2}{2\sigma^2}} \quad (3)$$

in which σ is the bandwidth of the generated photons. The state in equation (2) is sent to the input beamsplitter $BS1$, which, for simplicity, is described by the frequency independent amplitude reflectance and transmittance parameters r_1 and t_1 . The two arms of the MZ have different propagation losses γ_h and γ_r (defined as the ratio between the electric field at the input ports of $BS2$ and the electric field at the output ports of $BS1$), and a relative time delay $\Delta\tau$. The subscript h comes from the fact that we will use an electronic heater to vary $\Delta\tau$ in the experiment described in section 4, while the subscript r indicates the reference arm. The output beamsplitter $BS2$ has amplitude reflectivity r_{2j} and amplitude transmittivity t_{2j} , where $j = C, D$ refer to the output ports of $BS2$. This notation allows $BS2$ to be not symmetric with respect to the input beams A and B , e.g. the reflectivity from A to C (r_{2C}) can be different with respect to the reflectivity from B to D (r_{2D}). We point out that, in our case, such asymmetry is not attributed to an intrinsic unbalance of the $BS2$ transmittance/reflectance, but is induced by independently tuning the position of the focusing lenses in front of the detectors C and D . This is purposely done in order to introduce a given asymmetry in the interferometer and, therefore, to allow studying its effect in the coincidence rates. For both $BS1$ and $BS2$, we will assume an equal phase difference δ between the transmitted and reflected waves. The range of variability of δ , as discussed in appendix B, is determined by the magnitude of losses [17]. In the most familiar case of a lossless beamsplitter, $\delta = \pm\pi/2$ [18].

The electric fields E_C and E_D can be written as:

$$\begin{aligned} E_C^-(t) &= r_1 \gamma_h r_{2c} e^{-i2\delta} E_{in}^-(t - \Delta\tau) + t_1 \gamma_r t_{2c} E_{in}^-(t) \\ E_D^-(t) &= t_1 \gamma_r r_{2d} e^{-i\delta} E_{in}^-(t) + r_1 \gamma_h t_{2d} e^{-i\delta} E_{in}^-(t - \Delta\tau) \end{aligned} \quad (4)$$

where E_{in}^- is the negative frequency part of the input electric field operator at $BS1$. By inserting a completeness relation between $E_C^-(t + \tau)$ and $E_D^+(t + \tau)$ in equation (1), and by using equation (4) we find:

$$\begin{aligned} P(\tau) &= K |\gamma_{hc} \gamma_{rd} e^{-i3\delta} \langle E_{in}^-(t) E_{in}^-(t + \tau - \Delta\tau) \rangle \\ &\quad + \gamma_{rd} \gamma_{rc} e^{-i\delta} \langle E_{in}^-(t) E_{in}^-(t + \tau) \rangle \\ &\quad + \gamma_{hc} \gamma_{hd} e^{-i3\delta} \langle E_{in}^-(t - \Delta\tau) E_{in}^-(t + \tau - \Delta\tau) \rangle \\ &\quad + \gamma_{hd} \gamma_{rc} e^{-i\delta} \langle E_{in}^-(t - \Delta\tau) E_{in}^-(t + \tau) \rangle|^2 \end{aligned} \quad (5)$$

where the expectation values are now evaluated between the initial state $|\Psi_{\text{in}}\rangle$ and the vacuum state $|0\rangle$, i.e. $\langle E_{\text{in}}^-(t)E_{\text{in}}^-(t')\rangle = \langle \Psi_{\text{in}}|E_{\text{in}}^-(t)E_{\text{in}}^-(t')|0\rangle$. In equation (5) we have introduced the parameters:

$$\begin{aligned}\gamma_{hc} &= r_1 \gamma_h r_{2C} & \gamma_{hd} &= r_1 \gamma_h r_{2D} \\ \gamma_{rc} &= t_1 \gamma_r t_{2C} & \gamma_{rd} &= t_1 \gamma_r r_{2D}\end{aligned}\quad (6)$$

where the subscript h, r refers to the path along the upper or lower arm of the interferometer respectively, while subscript c, d denotes whether the photon arrives at detector C or D . The expectation values in equation (5) can be evaluated by using the Fourier representation of the negative frequency part of the input electric field:

$$E_{\text{in}}^-(t) = \int a_{\omega}^{\dagger} e^{i\omega t} d\omega \quad (7)$$

and hence that:

$$\langle E_{\text{in}}^-(t)E_{\text{in}}^-(t')\rangle = 2\phi(t-t')e^{i\tilde{\omega}t'} \quad (8)$$

where $\phi(t)$ is the Fourier transform of $\phi(\omega)$. Substituting equation (8) into equation (5), we obtain that $P(\tau) \propto |p_{h,h} + p_{r,r} + p_{h,r}^{(R)} + p_{h,r}^{(T)}|^2$, where:

$$p_{h,h} = 2r_1^2 t_{2D} r_{2C} \gamma_h^2 e^{-i(\tilde{\omega}\Delta\tau + 3\delta)} e^{-\frac{\sigma^2\tau^2}{2}} \quad (9)$$

$$p_{r,r} = 2t_1^2 t_{2C} r_{2D} \gamma_r^2 e^{-\frac{\sigma^2\tau^2}{2}} e^{-i\delta} \quad (10)$$

$$p_{h,r}^{(R)} = 2r_1 t_1 r_{2C} r_{2D} \gamma_h \gamma_r e^{-i(\frac{\tilde{\omega}\Delta\tau}{2} + 3\delta)} e^{-\frac{\sigma^2(\tau-\Delta\tau)^2}{2}} \quad (11)$$

$$p_{h,r}^{(T)} = 2r_1 t_1 t_{2C} t_{2D} \gamma_h \gamma_r e^{-i(\frac{\tilde{\omega}\Delta\tau}{2} + \delta)} e^{-\frac{\sigma^2(\tau+\Delta\tau)^2}{2}} \quad (12)$$

The amplitude probabilities in equations (9)–(12) are associated to well defined physical paths that the photon pair can follow from $BS1$ to ports C and D . These are sketched in figure 1. Consider for example the case in figure 1(a), which is described by equation (9): both signal and idler are reflected at $BS1$ and bunched into the upper arm of the MZ (r_1^2), and experience the same losses (γ_h^2). Then one photon is reflected to port C while the other is transmitted to the port D at $BS2$ ($t_{2D}r_{2C}$). While travelling in the upper arm, they acquire an overall phase factor $e^{-i\tilde{\omega}\Delta\tau}$. The factor $e^{-\frac{\sigma^2\tau^2}{2}}$ accounts for the fact that the two photons are localized in time within their coherence time $\tau_c = \frac{1}{\sigma}$. Similar reasoning applies to the cases when both photons are transmitted at $BS1$ (figure 1(b) and equation (10)) or when the pair is split (figures 1(c), (d) and equations (11)–(12)). The difference in the paths described by $p_{h,r}^{(R)}$ and $p_{h,r}^{(T)}$ comes from the fact that the pair reaches the output ports undergoing two reflections or two transmissions at $BS2$ respectively. The factor two in all the amplitude probabilities takes into account the fact that the system is symmetric for the exchange of signal and idler photons. It is worth noting that the coincidence measurement corresponds to an integration with respect to τ over the coincidence resolving time of a few nanoseconds of our detectors, which is much longer than the photon correlation time. After performing the modulus square of the sum of the four transition

amplitudes in equations (9)–(12) and integrating, one finds that the coincidence rate N_c is given by:

$$N_c(\Delta\tau) = K'(C_1 + C_2 + C_3) \quad (13)$$

where K' is a constant and the three terms on the right hand side are defined as follows:

$$C_1 = \gamma_{hc}^2 \gamma_{rd}^2 + \gamma_{hd}^2 \gamma_{rc}^2 + 2A_{\tilde{\omega}} e^{-\sigma^2\Delta\tau^2} \cos(2\delta) \quad (14)$$

$$C_2 = \gamma_{hc}^2 \gamma_{hd}^2 + \gamma_{rc}^2 \gamma_{rd}^2 + 2A_{\tilde{\omega}} \cos(\tilde{\omega}\Delta\tau - 2\delta) \quad (15)$$

$$\begin{aligned}C_3 &= 2e^{-\frac{\sigma^2\Delta\tau^2}{4}} \left[A_{\tilde{\omega}/2}^{(1)} \cos\left(\frac{\tilde{\omega}\Delta\tau + \delta}{2}\right) \right. \\ &\quad \left. + A_{\tilde{\omega}/2}^{(2)} \cos\left(\frac{\tilde{\omega}\Delta\tau}{2}\right) \right].\end{aligned}\quad (16)$$

In equations (14)–(16) we have adopted the following definitions:

$$A_{\tilde{\omega}} = \gamma_{rc} \gamma_{rd} \gamma_{hc} \gamma_{hd} \quad (17)$$

$$A_{\tilde{\omega}/2}^{(1)} = \gamma_{hc} \gamma_{rc} (\gamma_{rd}^2 + \gamma_{hd}^2) \quad (18)$$

$$A_{\tilde{\omega}/2}^{(2)} = \gamma_{hd} \gamma_{rd} (\gamma_{hc}^2 + \gamma_{rc}^2). \quad (19)$$

It is also convenient to introduce the power amplitude coefficient $A_{\tilde{\omega}/2}$ associated to the frequency component at $\frac{\tilde{\omega}}{2}$:

$$A_{\tilde{\omega}/2}^2 = (A_{\tilde{\omega}/2}^{(1)})^2 + (A_{\tilde{\omega}/2}^{(2)})^2 + 2A_{\tilde{\omega}/2}^{(1)}A_{\tilde{\omega}/2}^{(2)}\cos(2\delta). \quad (20)$$

Equation (14) represents the antibunching-antibunching interaction between the paths (c) and (d) in figure 1, resulting in the well-known HOM dip at the optical contact of the MZ ($\Delta\tau = 0$). Equation (15) describes the bunching-bunching interaction between the paths (a) and (b) in figure 1, which is mediated by the coupling strength $A_{\tilde{\omega}}$. This term oscillates at frequency $\tilde{\omega}$ which is two times the average single photon frequency ($\tilde{\omega}/2$) and is responsible of two photon interference. Finally equation (16) comes from the interference between the bunching cases with the antibunching ones, and is mediated by the interaction parameter $A_{\tilde{\omega}/2}$. This interference channel is missing in a balanced MZ or in a MZ which is fed symmetrically at the two input ports due to a completely destructive quantum interference [8, 12, 13]. This term shows fringes at $\tilde{\omega}/2$, creating a single photon interference pattern. This comes from the fact that the phase difference between the bunching and the antibunching cases is always $(\tilde{\omega}/2)\Delta\tau$. In fact, from the comparison of the paths (a-b) in figure 1 with the ones in figures 1(c)–(d), one can notice that there is always one arm of the interferometer which carries one more photon with respect to the other. The same happens when a single photon enters at the input of $BS1$: it can take either the lower arm or the upper one, giving a relative phase of $(\tilde{\omega}/2)\Delta\tau$ between the two paths. In general, the coincidence pattern exhibits competing effects between single and two particle interference, where their relative visibility can be evaluated by the magnitude of an *unbalancing*

parameter $\xi = A_{\omega/2}/A_{\omega}$. Without losing any generality, we can now restrict to the case of a lossless beamsplitter, in which $\delta = \frac{\pi}{2}$. In this case equation (20) simplifies to $A_{\omega/2}^2 = (\gamma_{hc}\gamma_{rd} - \gamma_{rc}\gamma_{hd})(\gamma_{hc}\gamma_{hd} - \gamma_{rc}\gamma_{rd})$.

In the limiting case where $\xi \rightarrow \infty$, the coincidence rate shows no signs of two photon correlations. This can occur when one of the four loss factor in equation (6) is equal to zero. If we consider for example the case $\gamma_{hc} = 0$, then the photon which fires the detector at port C is forced to come from the lower arm, providing a *which-path* information. The remaining uncertainty between the paths which the other photon of the pair may take to fire the other detector, gives raise to pure single photon interference. The lack of two photon correlations can be also explained from the fact that when $\gamma_{hc} = 0$, the bunching path in figure 1(a) is suppressed, so bunching-bunching interactions (which are the source of two photon correlations) cancel. In the opposite case where $\xi \rightarrow 0$, antibunching-bunching interactions cancel out. This happens when some symmetries are imposed on the arm losses or on the beamsplitter coefficients. The simplest case is when both the beamsplitters are 50/50 devices and the two arms have the same losses. We then have $\gamma_{hc} = \gamma_{hd} = \gamma_{rc} = \gamma_{rd}$ and consequently $A_{\omega/2} = 0$. Thus, only one frequency is observed when the device is ideal symmetric, which is consistent with what found in previous works [8, 12]. There exist actually three other possible configurations for which antibunching-bunching interactions cancel:

- i. Considering *BS2* perfectly balanced, in this case $\gamma_{hc} = \gamma_{hd}$ and $\gamma_{rd} = \gamma_{rc}$.
- ii. Imposing *BS1* balanced and, at the same time, the arm loss γ_r and γ_h to be equal, in this case $\gamma_{hc} = \gamma_{rc}$ and $\gamma_{rd} = \gamma_{hd}$.
- iii. Imposing that the transmittance from the input to port C while travelling in the upper arm is equal to the transmittance of its symmetric path ($\gamma_{rd} = \gamma_{hc}$) or vice-versa ($\gamma_{hd} = \gamma_{rc}$).

The presence of beamsplitter loss impeded a complete cancellation of the antibunching-bunching term. However, it is again the balanced configuration which minimizes this interference effect. Intermediate values of ξ can be realized by changing the relative arm transmittance.

3. Experimental setup

The model predictions of section 2 are validated using the experimental setup shown in figure 2.

Colour entangled photons near 1550 nm are generated by a 1 mm long PPLN crystal using a 775 nm continuous wave pump laser. Due to the small length of the crystal, the down-converted radiation is broadband, with a measured bandwidth of ≈ 300 nm. Type-0 SPDC allows to have co-polarized and collinear signal and idler photons. A long wavelength pass filter *IF* (1500 nm of cutoff wavelength) filters out the 775 nm pump from the infrared light, providing an isolation higher than 100 dB. In order to introduce a variable time delay

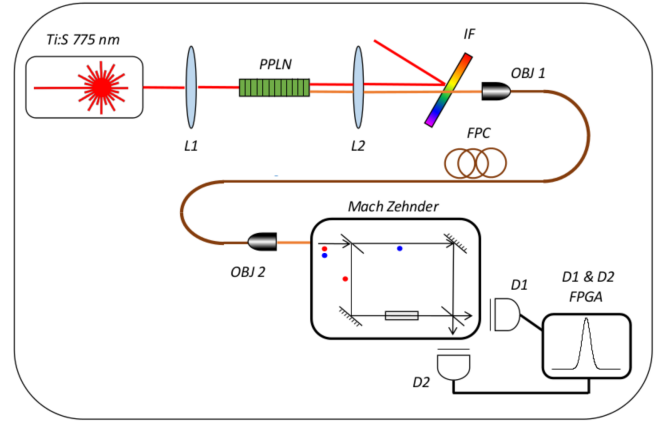


Figure 2. Outline of the experimental setup. L1,L2 = input/output lenses, PPLN = periodically poled lithium niobate, IF = interference filter, OBJ1,OBJ2 = input/output fiber couplers, D1, D2 = single photon detectors.

between the two arms of the interferometer, a cylinder of Borosilicate crown glass (NbK7) has been placed in both MZ arms. On one arm, the NbK7 is connected to an electric heater.

Thanks to the thermo-optic coefficient of the NbK7, we can smoothly vary the refractive index as a consequence of a change in the temperature. We are able to induce a slow linear increase of the time delay between the arms which can be as long as 180 fs in a four hours measurement. This time delay has been extracted by assuming a central wavelength of the SPDC radiation of 1550 nm, which corresponds to a fringe period of 5.16 fs. The smoothness of the refractive index change and the long duration of the measurement allows to reduce the noise of the apparatus and to produce high quality coincidence fringes with relative low counts (< 10 Hz). The photons at the output ports of the interferometer are focused by two lenses onto two InGaAs single photon counting detectors D1 and D2 (ID Quantique Id210 and ID Quantique Id201). D1 works in free running mode (40 μ s of deadtime) and has the task to herald one photon of the pair. D2 is triggered by D1 and is enabled for a gate width of 100 ns. The outputs of the photodiodes are fed into a field programmable gate array digital correlator that provides the coincidence rate. The coincidence window is 5 ns.

4. Measurements

The single port (in this case, port D) count rate is measured as a function of the time delay $\Delta\tau$ and is shown in figure 3. Since the curve is symmetric with respect to the optical contact, we report only the measured values for negative time delays.

As expected, the curve exhibits oscillations with a period equal to $\frac{2\pi}{\omega/2}$, since it comes from single particle interference. These oscillations are modulated by a slowly varying

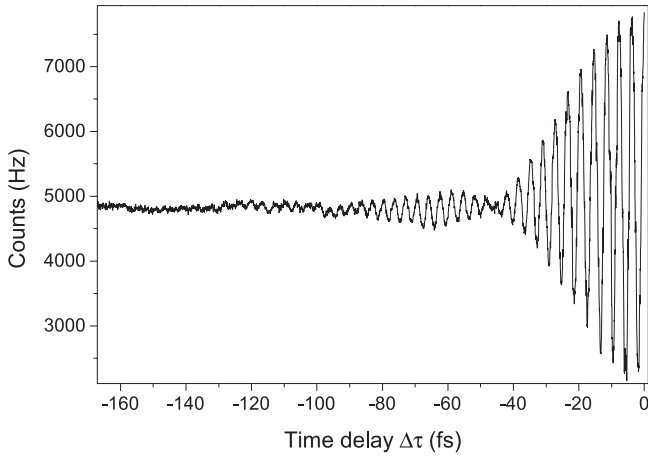


Figure 3. The single port count rate for port *D* is shown as a function of the interferometer time delay $\Delta\tau$. The optical contact, where the two arms have no time delay, is placed at $\Delta\tau = 0$

envelope due to the finite coherence time of the photons, through which we estimated a value of τ_c of $(24.1 \pm 0.7)fs$. We notice that the oscillations do not damp immediately to zero for $\Delta\tau \gg \tau_c$, but exhibits a ripple. This is due to the presence of the interference filter *IF*, which has an abrupt decrease of the transmittance at 1500 nm, as well as to the roll off of the detector efficiency, which occurs at 1650 nm. As a result, the spectral distribution of the photons entering the MZ is box-like, and shows an autocorrelation which resembles a *sinc* function. However, the gaussian distribution in equation (3) will be kept during the rest of this section since it provides an excellent approximation. The coincidence rate obtained for different values of the unbalancing parameter ξ is shown in figure 4. To change the value of ξ , we simply independently tune the position of the focusing lenses in front of the detectors *C* and *D*. The values of ξ reported in figure 4 are taken from simulation. In the case $\xi = 0.77$ in figure 4, we balanced the interferometer in order to suppress antibunching-bunching interactions. The residual component at $\tilde{\omega}/2$ is only due to the beam splitter losses (approximately 22%, as discussed in appendix B). The coincidence rate exhibits practically the same oscillating behaviour at frequency $\tilde{\omega}$ within and outside the coherence time of the single photons. The observed pattern becomes a mixture between bunching-bunching and HOM-like interference. The latter manifests itself as a decrease in the average value of the coincidence counts as we approach the optical contact. The oscillation in the coincidence rate outside the coherence time is a clear manifestation of the correlated orentangled nature of the two-photon state created in the down conversion process [12]. To clearly show that the oscillation at frequency $\tilde{\omega}$ is due to purely second order interference effects, we plot in the inset of figure 4 (panel $\xi = 1.34$) the coincidence rate for time delays greatly exceeding the single photon coherence time ($\Delta\tau > 100 fs$). As we can see from figure 3, for such time delays any possible contribution arising from first order interference to the coincidence pattern vanishes. Even if not reported in figure 4, the very same oscillations outside τ_c are observed regardless of the value of ξ .

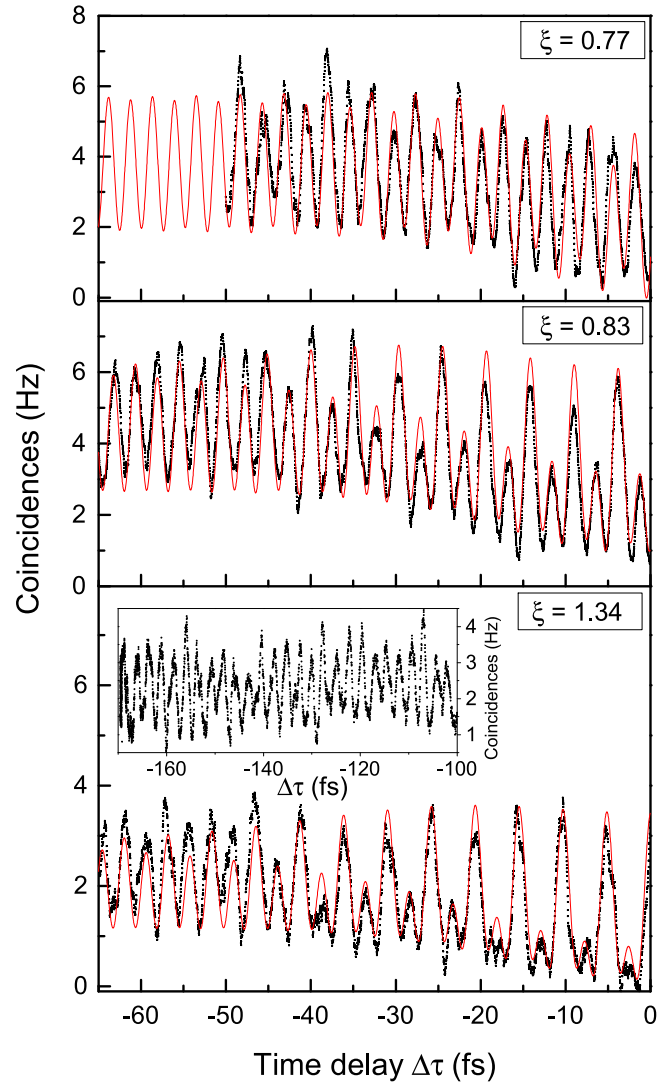


Figure 4. The coincidence photodetection rate is plotted against the interferometer time delay $\Delta\tau$ for different values of the unbalancing parameter ξ . The solid red curves represent equation (13), while black scatters are experimental data. The inset shown in the panel $\xi = 1.34$ shows the coincidence rate for time delays larger than the single photon coherence time. The reported value of ξ is taken from the simulation. A value of $\delta \approx 0.87\frac{\pi}{2}$ has been used, which is compatible with a measured beamsplitter loss of $\approx 22\%$ (see appendix B and ref. [17]). Values of the fit parameters are reported in appendix A.

As ξ is increased, the pattern changes significantly with respect to the balanced situation, due to the enabling of new interference paths. The case at $\xi = 0.83$ in figure 4 includes two photon, one photon and Hong Ou Mandel interference effects all in a single coincidence pattern. Indeed, outside the coherence time, the antibunching terms in figures 1(c)–(d) have vanishing probability, so the interference fringes at $\tilde{\omega}$ are due to purely two photon correlation effects. Within the coherence time of the photon wave packet, instead, the paths (c) and (d) in figure 1 are allowed to interfere together with the ones in (a) and (b), creating a mixed pattern in which single particle interference at $\tilde{\omega}/2$ and two particle one at $\tilde{\omega}$ coexist. The HOM effect again can be seen as the decrease of the average coincidences within the coherence time. In general the higher is the unbalancing

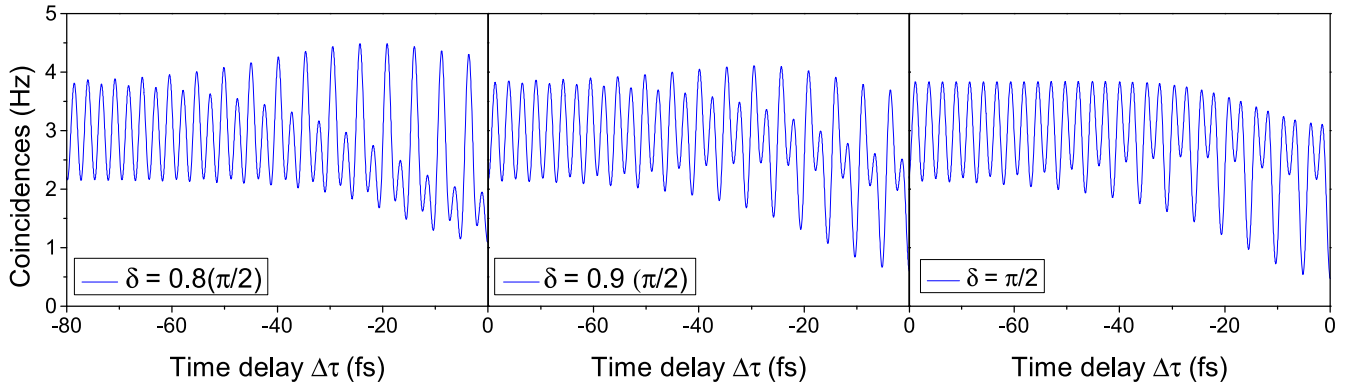


Figure 5. Effect of the beamsplitter induced phase δ on the coincidence pattern.

between the arms, the higher is the suppression of the two-photon contribution at $\tilde{\omega}$ and, at the same time, the higher the visibility of the single-photon component at $\tilde{\omega}/2$. We see from figure 4 that it is sufficient to induce a value of $\xi = 1.34$ to practically cancel out the oscillation at $\tilde{\omega}$ within the coherence time. In all the three cases shown in figure 4, simulations (solid red curves) well matches the experiment only if the phase δ slightly deviates from $\frac{\pi}{2}$ ($\delta = 0.87\frac{\pi}{2}$), i.e, if one assume that the beamsplitter is lossy (see appendix B). The high sensitivity to (even small) phase changes induced by the beamsplitter is shown in figure 5. Here, patterns have been simulated using the same experimental parameters as in the case $\xi = 1.34$ in figure 4. We clearly see that a lossless BS ($\delta = \frac{\pi}{2}$) do not correctly model the experimental patterns in figure 4. With a 20% deviation of δ from $\frac{\pi}{2}$, the fringe pattern gets mirrored-like with respect to the lossless case. This high sensitivity comes from the fact that the BS phase δ enters in the three path-interactions terms in equations (14)–(16) with different combinations, so that even small variations can significantly alter the coincidence rate.

5. Conclusions

We have re-analyzed the well-known Mach-Zehnder interferometer by considering asymmetry and losses in the propagation of the photons. We have shown a quantum mechanical effect where, by independently tuning the global transmittance of the arms of a free space Mach-Zehnder interferometer, we can actually control the degree of interference between bunching and anti-bunching states leading to a coincidence photodetection. In this experiment a correlated pair of signal and idler photons, produced by SPDC, is sent at the same input port of the interferometer. This configuration ensures the possibility to reveal, on the same coincidence pattern, signs of one photon, two photon and HOM-like interference effects. The experimental results are in very good agreement with theory. We think that our treatment offers an improved comprehension and a more general view of the MZ interferometer, which for all practical applications (both free space or integrated) faces the problem of amplitude

unbalancing due to spatial misalignments, propagation losses or fabrication errors. The theoretical method developed can be directly applied as it stands to an integrated MZ on a chip, provided that the phase velocity in free space is replaced with the phase velocity in the guided geometry. Furthermore, even if not explicitly treated in this work, we point out that in principle similar effects could be observed in all interferometric structures based on beam amplitude division.

Acknowledgments

We wish to thank dott. Iacopo Carusotto (INO-CNR BEC of Trento) for the helpful discussions.

This research is supported by Provincia Autonoma di Trento by the SiQuoro project.

Appendix A. Fit parameters of the coincidence rate

A stochastic algorithm (differential evolution optimization [19]) has been adopted to minimize the cost function in equation (13). We choose γ_{hd} , γ_{hc} , γ_{rd} , γ_{rc} , σ , δ , K' as free parameters. The frequency $\tilde{\omega}$ has been fixed to $\tilde{\omega} = 2.448 \text{ fs}^{-1}$, which corresponds to a wavelength of $\tilde{\lambda} = 775 \text{ nm}$.

We run the algorithm 15 times in order to improve the accuracy of the parameters. Each run has been stopped after a fixed number of iterations (600). Further iterations were seen to not significantly improve the goodness of the fit (the discrepancy decreases about the 0.001% by doubling the number of iterations). The values of the optimized parameters are listed in table 1. Since the value of σ does not depend on ξ , it has been computed only for $\xi = 1.34$ and then kept fixed during the optimization of the cases $\xi = 0.77$ and $\xi = 0.83$. The minimum loss measured from the input port of the Mach Zehnder to the two detectors is $\approx 7 \text{ dB}$, which is comparable to the value found in the simulation (minimum loss of $\approx 9 \text{ dB}$).

Table 1. List of the coefficients minimizing the discrepancy between the experimental data in figure 4 and the curve generated by equation (13).

Parameter	$\xi = 0.77$ (Upper panel)	$\xi = 0.83$ (Middle panel)	$\xi = 1.34$ (Lower panel)
K' [fs ⁻¹]	1.8 ± 0.1	3.6 ± 0.4	12 ± 1
σ^{-1} [fs]		24.1 ± 0.7	
δ [rad]		1.37 ± 0.04	
γ_{hd}	0.47 ± 0.01	0.300 ± 0.001	0.124 ± 0.005
γ_{hc}	0.65 ± 0.02	0.66 ± 0.04	0.55 ± 0.02
γ_{rd}	0.64 ± 0.02	0.500 ± 0.001	0.36 ± 0.01
γ_{rc}	0.65 ± 0.02	0.66 ± 0.03	0.35 ± 0.01
$A_{\tilde{\omega}/2}$	$(9.7 \pm 0.7) \cdot 10^{-2}$	$(5.41 \pm 0.3) \cdot 10^{-2}$	$(1.14 \pm 0.04) \cdot 10^{-2}$
$A_{\tilde{\omega}}$	(0.125 ± 0.002)	$(6.5 \pm 0.2) \cdot 10^{-2}$	$(8 \pm 1) \cdot 10^{-3}$
ξ	0.77 ± 0.05	0.83 ± 0.04	1.34 ± 0.05

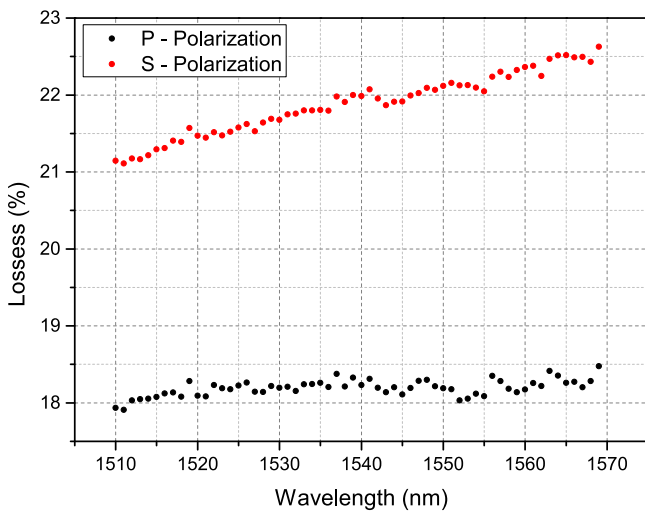


Figure 6. Beamsplitter lossess for P and S polarized waves.

Appendix B. Beamsplitter loss and phase

The beamsplitter losses and the relative phase between the transmitted and reflected waves play a significant role in our measurements. Figure 6 shows the measured BS lossess for both S and P polarized waves in the wavelength range 1510 nm–1570 nm. We worked with S polarized photons in our experiment. This corresponds to an average loss of $(21.9 \pm 0.4) \%$ for each BS. If the BS were lossless, the relative phase δ between the transmitted and the reflected wave at the output ports will be fixed to $\delta = \frac{\pi}{2}$. When lossess are introduced, this constraint relaxes to the inequality [17]:

$$|\cos(\delta)| \leq \frac{1}{\gamma} - 1 \quad (21)$$

where $\gamma = |r|^2 + |t|^2$. In deriving equation (21), we assumed a 50/50 BS with real transmittance $t = \sqrt{\frac{\gamma}{2}}$ and complex reflectance $r = te^{i\delta}$. This simplified model describes quite

well the BS in our experiment. By setting $\gamma = 0.781$ in equation (21) we found that the phase δ must be bounded between $\delta_{\min} = (1.287 \pm 0.007)\text{rad}$ and $\delta_{\max} = (1.855 \pm 0.007)\text{rad}$. These constraints have been imposed to δ during the optimization procedure described in the previous section. The value which best fits our data has been found to be $(1.37 \pm 0.04)\text{rad}$.

References

- [1] Pan J W, Chen Z B, Lu C Y, Weinfurter H, Zeilinger A and Zukowski M 2012 *Rev. Mod. Phys.* **84** 777
- [2] Kaiser F et al 2014 *Opt. Commun.* **327** 7
- [3] Walborn S P, Terra Cunha M O, Padua S and Monken C H 2002 *Phys. Rev. A* **65** 033818
- [4] Giovannetti V, Lloyd S and Maccone L 2004 *Science* **306** 1330
- [5] Hong C K, Ou Z Y and Mandel L 1987 *Phys. Rev. Lett.* **59** 2044
- [6] Franson J D 1989 *Phys. Rev. Lett.* **62** 2205
- [7] Kwiat P G, Vreka W A, Hong C K, Nathel H and Chiao R Y 1990 *Phys. Rev. A* **41** 2910
- [8] Rarity J G, Tapster P R, Jakeman E, Larchuk T, Campos R A, Teich M C and Saleh B E A 1990 *Phys. Rev. Lett.* **65** 1348
- [9] Politi A, Cryan M J, Rarity J G, Yu S and O'Brien J L 2008 *Science* **320** 646
- [10] Silverstone J W et al 2014 *Nat. Phot.* **8** 104
- [11] Bonneau D, Engin E, Ohira K, Suzuki N, Yoshida H, Iizuka N, Ezaki M, Natarajan C M, Tanner M G and Hadfield R H 2012 *New J. Phys.* **14** 045003
- [12] Campos R A, Saleh B E A and Teich M C 1990 *Phys. Rev. A* **42** 4127
- [13] Paris M 1999 *Phys. Rev. A* **59** 1615
- [14] Shih Y H, Sergienko A V, Rubin M H, Kiess T E and Alley C O 1994 *Phys. Rev. A* **49** 4243
- [15] Rarity J G and Tapster P R 1989 *J. Opt. Soc. Am. A* **6** 1221
- [16] Helt L G, Liscidini M and Sipe J E 2012 *J. Opt. Soc. Am. B* **29** 2199–212
- [17] Barnett S M, Jeffers J, Gatti A and Loudon R 1998 *Phys. Rev. A* **57** 2134
- [18] Zeilinger A 1981 *Am. J. Phys.* **49** 882
- [19] Rainer S and Price K 1997 *J. Global Optim.* **11** 341